Automatic Nuclei Detection based on Generalized Laplacian of Gaussian Filters

Hongming Xu, Cheng Lu, Richard Berendt, Naresh Jha, and Mrinal Mandal, *Senior Member, IEEE*

Abstract—Efficient and accurate detection of cell nuclei is an important step towards automatic analysis in histopathology. In this work, we present an automatic technique based on generalized Laplacian of Gaussian (gLoG) filter for nuclei detection in digitized histological images. The proposed technique first generates a bank of gLoG kernels with different scales and orientations, and then performs convolution between directional gLoG kernels and the candidate image to obtain a set of response maps. The local maxima of response maps are detected and clustered into different groups by mean-shift algorithm based on their geometrical closeness. The point which has the maximum response in each group is finally selected as the nucleus seed. Experimental results on two datasets show that the proposed technique provides a superior performance in nuclei detection compared to existing techniques.

Index Terms—Nuclei detection, Laplacian of Gaussian filter, mean-shift algorithm, thresholding

I. INTRODUCTION

ROBUST nuclei detection is an important step in histopathology for disease diagnosis, as the counts of nuclei provide quantitative information when studying changes in cells, tissues and organs [1], [2]. For example, the density of cell nuclei in histological images is an important feature for automatic breast tumor grading [3]. In addition, nuclei detection is usually the first step for nuclei segmentation [4], [5], and the accuracy of segmentation depends critically on the accuracy and reliability of the detected points (i.e., seed points) [6].

With recent advances in digital imaging and machine intelligence, enormous research efforts have been devoted to the development of automatic nuclei detection and segmentation [7], [8], [9]. Thresholding-based techniques have been well-studied for identifying nuclei numbers and locations [3], [10], but they have limitations in locating clustered nuclei. To detect clustered nuclei, Cheng et al. [11] proposed an adaptive H-minima transform technique that detects nuclei by adaptively suppressing the local minima from the inner distance map. Jung et al. [12] further formulated the nuclei detection based on H-minima transform as an optimization problem, which

H. Xu and M. Mandal are with the Department of Electrical and Computer Engineering, University of Alberta, Edmonton, AB, T6G 1H9 Canada (e-mail: mxu@ualberta.ca, mmandal@ualberta.ca).

C. Lu is with the Department of Biomedical Engineering, Case Western Reserve University, OH, 44106 USA. C. Lu is supported by the National Natural Science Foundation of China (Grant No.61401263) and Natural Science Basic Research Plan in Shaanxi Province of China (Program No.2015JQ6228) (e-mail: chenglu@snnu.edu.cn).

R. Berendt and N. Jha are with the Department of Oncology, Cross Cancer Institute, University of Alberta, Edmonton, AB, T6G 1Z2 Canada (e-mail: richard.berendt@albertahealthservices.ca, naresh.jha@albertahealthservices.ca).

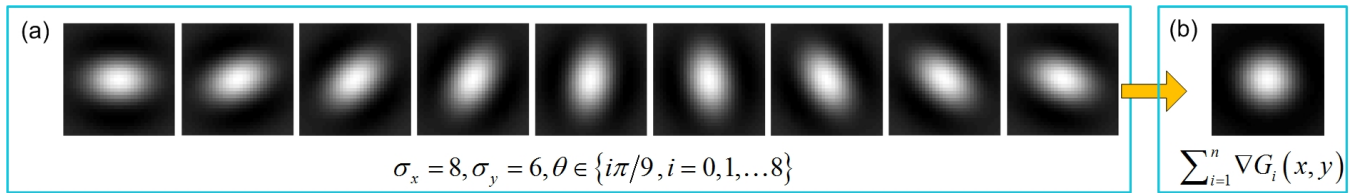determines an optimal depth value (corresponds to the minimum fitting error) to suppress the undesired local minima in the distance map. Parvin et al. [13] proposed a multi-pass voting technique for inferring the centers of cell nuclei. This technique initially votes along the gradient direction of high gradient pixels in a cone-shape voting area, and then iteratively votes in multiple passes with a shrunk voting area and updated voting direction (towards the highest votes in the previous pass). The points which have the votes above a predefined threshold are finally considered as nuclei seeds. To speed up the multiple-pass voting in [13], Qi et al. [4] proposed a single-pass voting technique for nuclei detection, which only performs a single-pass voting followed by mean shift clustering to detect nuclei seeds. Xu et al. [5] further improved single-pass voting algorithm by voting along nuclei boundaries and distributing votes with a Gaussian kernel in nuclei regions. Although these techniques have been reported to provide a good performance, they are either sensitive to the predefined parameters or have high computational complexity. They tend to be infeasible for high-throughput analysis of images with a large number of cell nuclei.

Since cell nuclei typically have circular shapes, they can be considered as blob-like structures which can be detected efficiently using scale-space theory. For detecting blob-like objects, Lindeberg [14] provided an elegant method that first convolves the image with the normalized Laplacian-of-Gaussian (LoG) filters at varying scales to form a scale-space representation, and then detects scale-space extrema as blob seeds. Lowe [15] approximated the normalized LoG filters with difference-of-Gaussian (DoG) filters and also detected objects as local extrema in scale-space. The DoG scale-space representation is obtained by subtracting two successive Gaussian smoothed images, which is more efficient than LoG operation. Based on the scale-space theory, Byun et al. [1] proposed a nuclei detector in retinal images that performs nuclei detection with a single-scale LoG filter. This method has a low computational complexity, but it fails to provide a good performance when the candidate image has nuclei with different sizes and shapes. Niazi et al. [16] proposed to detect cytotoxic T-cells seeds by multi-scale DoG filters, with false seeds removed based on blobness measurement [17]. Al-Kofahi et al. [18] proposed a multi-scale LoG filters (mLoG) based technique for nuclei detection, which first extracts image foreground with a graph-cuts-based binarization, and then detects nuclei seeds by mLoG filtering with a distance-map-constrained adaptive scale selection.

The aforementioned LoG operators have shown a promising performance in locating the seeds of circular blobs, but they

Fig. 1. Summation of gLoG kernels. (a) 9 directional gLoG kernels. (b) The summation result. Note that σ_x and σ_y are the scales of the gLoG kernel, and θ determines the orientation of the gLoG kernel.

have limitations in detecting blobs with general elliptical shapes. This is because the conventional LoG operators are generated from the uniform Gaussian kernels which are rotational symmetric in all directions. In order to identify elliptical blob structures and their scales, Okada et al. [19] proposed a method for creation of the anisotropic Gaussian scale-space, which has been used to the problem of estimating anisotropic spreads of pulmonary tumors. Mikolajczyk and Schmit [20] proposed a multi-scale Harris interest point detector, which searches interest points in an affine Gaussian scale space. Recently, Kong et al. [21] proposed a gLoG filter based algorithm for detecting elliptical blob centers (e.g., nuclei seeds) in images. The algorithm first generates a set of log-scale-normalized gLoG kennels, $\nabla^2 G_i(x,y), i = 1 \ldots n$, with different scales and orientations. The convolution of each gLoG kernel and the image $I(x,y)$ is then performed, and an aggregated response map L_s is obtained by summing up all intermediate response maps, i.e.,

$$L_s = \sum_{i=1}^{n} \left(\nabla^2 G_i(x,y) * I(x,y) \right) \tag{1}$$

where $*$ is the convolution operation. The spatially local maxima in the aggregated response map L_s are finally detected as blob centers. Note that Eq. (1) can be reformulated, based on the distributivity property of the convolution operation [22], as:

$$L_s = I(x,y) * \sum_{i=1}^{n} \nabla^2 G_i(x,y) \tag{2}$$

The computational complexity of Eq. (2) is much lower than that of Eq. (1), as the times of convolution operations have been greatly reduced (from n to 1). Actually, the summation of different directional gLoG kernels together, like in Eq. (2), essentially results in a LoG kernel. For example, Fig. 1(a) shows a set of 9 directional gLoG kernels with scales $\sigma_x = 8$ and $\sigma_y = 6$. Fig. 1(b) shows the summation of gLoG kernels in Fig. 1(a), which is essential a LoG kernel. From Fig. 1, it can be seen that the directional information of gLoG kernels have been lost during the generation of the aggregated response map by Eq. (1) in [21]. Since the blob location algorithm in [21] have not taken the advantage of gLoG kernels's directional information, it is likely to miss seeds for nuclei regions that do not have peak responses in the aggregated response map. Besides, the algorithm in [21] is quite sensitive to the local noise in the image background [23], as it considers all local maxima in the aggregated response map as blobs seeds. Fig. 2 shows an example of nuclei detection in a hematoxylin and eosin (H&E) stained skin image using the algorithm in [21],

where the automatically detected nuclei seeds are indicated by (green) plus symbols. Note that the (red) rectangles highlight the missed nuclei (without seeds), while the (blue) circles highlight the false seeds (due to noisy pixels).
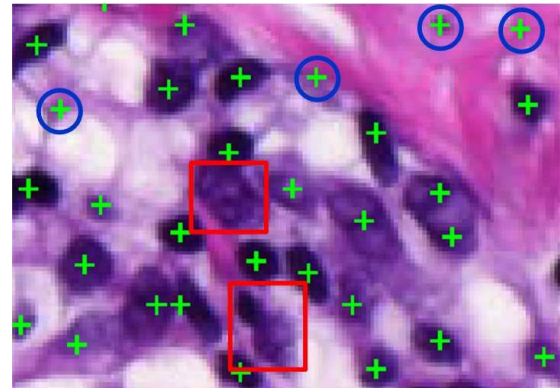

Fig. 2. Nuclei detection results by the algorithm in [21]. Note that (green) plus symbols indicate the detected nuclei, whereas (red) rectangles and (blue) circles highlight the missed nuclei and false seeds, respectively.

In this paper, we propose an efficient and accurate technique for nuclei detection in microscopic images, which overcomes many of the limitations of the existing techniques. The main contribution of this work is that a computationally efficient nuclei seeds detection algorithm based on directional gLoG kernels and mean-shift clustering is proposed. This algorithm searches nuclei seeds from multiple response maps obtained by convolving directional gLoG kernels with the image. False seeds in the image background are removed based on adaptive thresholding, and redundant seeds are merged based on mean-shift clustering. The organization of this paper is as follows. Section II illustrates image dataset used in this work. Section III describes the proposed technique, followed by the performance evaluations in Section IV. The conclusion is presented in Section V.

II. DATASET DESCRIPTION

This study was based on two datasets of H&E stained histopathology images. The first dataset (dataset-I) is collected from the cross cancer institute, University of Alberta in accordance with the protocol for examination of specimens with skin melanoma. The skin biopsies contained melanocytic nevi and skin melanomas. The original skin images were captured under 40X magnification on Carl Zeiss MIRAX MIDI scanning system. The first dataset (Dataset-I) includes 12 skin histopathological images, which were cropped skin

epidermis-dermis junction regions from six whole slide images (i.e., 2 images are cropped from each whole slide image). These cropped images were saved in TIFF format with 10X magnification for a good balance between image quality and size. The 12 images on average have a size of 1326×667 pixels, and have a total of 7,701 cell nuclei. The second dataset (Dataset-II) is a published online dataset [24], which consists of 18 breast histopathology images. The 18 breast images on average have a size of 896×768 pixels, and have a total of 6,048 cell nuclei. Although datasets I and II consist of color images, this work uses the red channel image, as it provides a good contrast between nuclei and background in H&E stained images [10], [25].

III. PROPOSED TECHNIQUE

The schematic of the proposed technique for nuclei detection is shown in Fig. 3. It is observed that there are three modules. In the first module, a bank of scale-normalized gLoG kernels with different scales and orientations are constructed. In the second module, the constructed gLoG kernels are summed together according to their orientations, and the response maps are generated by convolving the summed gLoG kernels with the image. In the third module, the nuclei seeds are detected from multiple response maps with redundant detections merged by mean-shift clustering. The details of three modules are now presented in the following.
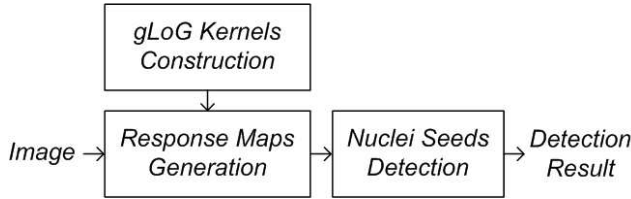

Fig. 3. Schematic of the proposed technique.

A. gLoG Kernels Construction

Because cell nuclei in digitized histopathological images typically have circular or elliptical shape, the gLoG kernels (see Fig. 1) are appropriate for nuclei detection. In this work, we use a bank of gLoG kernels with different scales and orientations for nuclei identification. To make the article self-contained, in this module we illustrate the gLoG kernels construction and show that traditional scale-normalization for gLoG kernels performs better than log-scale normalization in [21]. The gLoG kernel $\nabla^2 G(x, y)$ is given as follows:

$$\nabla^2 G(x, y) = \frac{\partial^2 G(x, y)}{\partial x^2} + \frac{\partial^2 G(x, y)}{\partial y^2} \tag{3}$$

where (x, y) are the image domain coordinates, $G(x, y) = \lambda \cdot e^{-\left(ax^2 + 2bxy + cy^2\right)}$, and the Laplacian $\partial^2 G(x, y)/\partial x^2$, $\partial^2 G(x, y)/\partial y^2$ are given by:

$$\frac{\partial^2 G(x, y)}{\partial x^2} = \left[(2ax + 2by)^2 - 2a\right] G(x, y) \tag{4}$$

$$\frac{\partial^2 G(x, y)}{\partial y^2} = \left[(2bx + 2cy)^2 - 2c\right] G(x, y) \tag{5}$$

TABLE I
INDEX OF GLoG KERNELS' CONFIGURATION.

Index	σ_x, σ_y	θ (degree)	Index	σ_x, σ_y	θ (degree)
1	8,8	0	2-5	8,7	0,45,90,135
6-9	8,6	0,45,90,135	10-13	8,5	0,45,90,135
14-17	8,4	0,45,90,135	18	7,7	0
19-22	7,6	0,45,90,135	23-26	7,5	0,45,90,135
27-30	7,4	0,45,90,135	31	6,6	0
32-35	6,5	0,45,90,135	36-39	6,4	0,45,90,135
40	5,5	0	41-44	5,4	0,45,90,135
45	4,4	0			

where λ is a normalization factor and the parameters a, b, c control the shape and orientation of the gLoG kernel, which are defined as follows [21]:

$$a = \frac{\cos^2\theta}{2\sigma_x^2} + \frac{\sin^2\theta}{2\sigma_y^2} \tag{6}$$

$$b = -\frac{\sin 2\theta}{4\sigma_x^2} + \frac{\sin 2\theta}{4\sigma_y^2} \tag{7}$$

$$c = \frac{\sin^2\theta}{2\sigma_x^2} + \frac{\cos^2\theta}{2\sigma_y^2} \tag{8}$$

where (σ_x, σ_y) are the scales and θ is the orientation of the gLoG kernel. By varying the scales and orientations, a set of different gLoG kernels $\nabla^2 G(x, y)$ can be obtained. To construct a bank of gLoG kernels for nuclei identification, we first set angles that the gLoG kernel's orientation can take, which is as follows:

$$\theta = \frac{\pi}{k}(i - 1), \quad i = 1 \ldots k \tag{9}$$

where k is the number of orientations. The range of scales σ_x and σ_y are then set as positive integers between $\sigma_{\min}$ and $\sigma_{\max}$, where $\sigma_{\min}$ and $\sigma_{\max}$ are determined based on the estimated radius of detected nuclei [26]. Without loss of generality, we assume that $\sigma_x \geq \sigma_y$. Table I shows an example of gLoG kernels' configuration, where θ has 4 orientations and $4 \leq \sigma_y \leq \sigma_x \leq 8$.
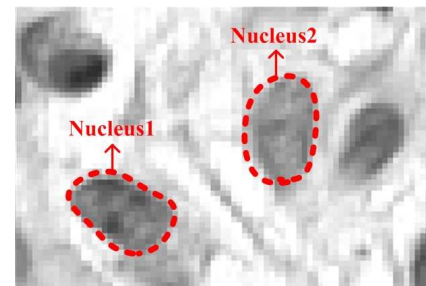

Fig. 4. Nuclei in a skin image. Note that the orientations for nucleus1 and nucleus2 are about 135° and 90°, respectively. The ratios between σ_x and σ_y for both nuclei are about 2.

When convolving gLoG kernels with the image containing blobs with general elliptical shapes, it produces a scale-and-orientation selective peak response at the center of each object. This can be considered as a pattern matching process, which
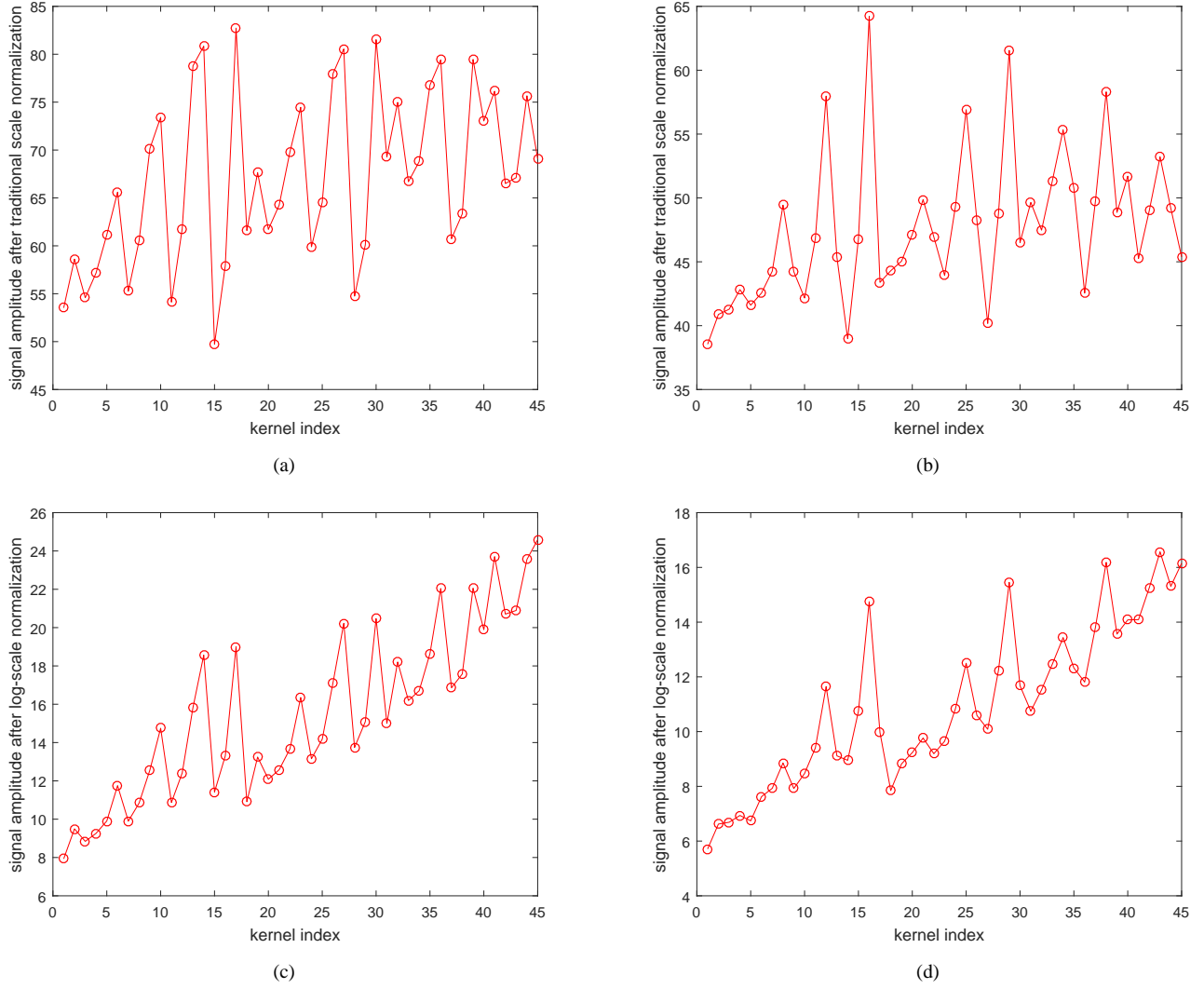
Fig. 5.   Peak responses by traditional scale normalization and log-scale normalization. (a) and (b) Peak responses at nucleus1 and nucleus2 shown in Fig. 4 using traditional scale normalization (by Eqs. (10)&(12)). (c) and (d) Peak responses at nucleus1 and nucleus2 shown in Fig. 4 using log-scale normalization (by Eqs. (11)&(12)). Note that the kernel index in the horizontal axis has been shown in Table I.

matches the predefined gLoG kernels of different scales and orientations to the given image patterns. However, a direct application of multi-scale gLoG kernels to images of blobs would be unreliable, since the signal amplitude of the gLoG convolution at blob regions decreases monotonically as the scales increase. A straightforward way to keep the signal amplitude invariant across changes of image scale is to apply the scale normalization. Lindeberg [14] proposed a traditional normalization method for the LoG filter. This normalization method has been used by Xiao et al. [27] for curvilinear structures detection using the bi-Gaussian kernel. For the scale normalization of gLoG filters in this work, the traditional normalization method in [14] can be intuitively extended and defined as:

$$\nabla^2 G_n (x,y) = \sigma_x \sigma_y \nabla^2 G (x,y) \tag{10}$$

where $\nabla^2 G_n (x,y)$ is the scale-normalized gLoG kernel. Kong et al. [21] proposed a log-scale normalization for gLoG filter,

that is:

$$\nabla^2 G_n (x,y) = (1 + \alpha \log (\sigma_x)) (1 + \alpha \log (\sigma_y)) \nabla^2 G (x,y) \tag{11}$$

where α is a positive number (e.g., $\alpha = 0.5$) which can control the eccentricities of detected blobs. To evaluate the capacity of scale normalization by Eq. 10 and Eq. 11, we have separately applied the traditional scale normalized gLoG kernels and log-scale normalized gLoG kernels on our testing images, i.e.,

$$L_n (x,y) = \overline{I} (x,y) * \nabla^2 G_n (x,y) \tag{12}$$

where $I (x,y)$ is the original red channel image and $\overline{I} (x,y) = 255 - I (x,y)$. $L_n (x,y)$ is the convolution response map. Note that the nuclei regions appear as dark blobs in the original red channel image, and hence the complement operation in Eq. (12) is performed to make nuclei regions as bright foreground. Fig. 4 shows cell nuclei in a testing skin image, where the orientations of nucleus1 and nucleus2 are about $135°$ and $90°$, respectively and the ratios between

TABLE II
INDEX OF NORMALIZED GLOG KERNELS WITH MAXIMUM RESPONSES.

Nuclei	Traditional normalization			Log-scale normalization		
	Index	σ_x, σ_y	θ	Index	σ_x, σ_y	θ
Nucleus1	17	8,4	135°	45	4,4	0°
Nucleus2	16	8,4	90°	43	5,4	90°

σ_x and σ_y for both nuclei are about 2. Figs. 5(a)(b) show the maximum convolution responses by applying traditional scale-normalized gLoG kernels (using Eq. (12)) on nucleus1 and nucleus2, respectively. Figs. 5(c)(d) show the maximum convolution responses by applying log-scale normalized gLoG kernels ($\alpha = 1$) on nucleus1 and nucleus2, respectively. The kernel index (in horizontal axis) of Fig. 5 has been provided in Table I. As observed in Figs. 5(a)(b), the maximum responses are obtained when the kernel indices are 17 and 16 respectively. By contrast, in Figs. 5(c)(d) the maximum responses are obtained when the kernel indices are 45 and 43 respectively. Table II shows gLoG kernel's configurations which provide the maximum responses using different normalization methods. As shown in Table II, it is apparent that the traditional scale normalization performs better than log-scale normalization, since the traditional normalized gLoG kernel with the maximum response has a good matching with the cell nucleus. Therefore, in this work, we utilized the traditional normalization on gLoG kernels (see Eq. (10)) for nuclei detection. Figs. 6(a)(b) show examples of traditional normalized gLoG kernels with scales between $[8, 8]$ and $[4, 4]$ in 4 directions. As observed in Fig. 6(a), the gLoG kernels are rotational-symmetric when $\sigma_x = \sigma_y$, which are essentially the LoG kernels.

B. Response Maps Generation

After constructing a set of normalized gLoG kernels, the next is to convolve the image with gLoG kernels to obtain response maps which provide information about nuclei numbers and locations. Although it is possible to do the convolution between each gLoG kernel and the image (like the blob localization algorithm in [21]), it is time-consuming due to multiple convolutions. To speed up the algorithm, we make use of distributivity property of convolution operation and compute the summation of gLoG kernels before convolution operation. Specifically, for the rotational symmetric gLoG kernels (see Fig.6(a)), the summed gLoG filter $\nabla^2 G_s (x, y)$ is given by:

$$\nabla^2 G_s (x, y) = \frac{1}{S_0} \sum_{\sigma=\sigma_{\min}}^{\sigma_{\max}} \nabla^2 G_n (x, y; \sigma) \qquad (13)$$

where S_0 is the number of summed rotational symmetric gLoG kernels. For other general elliptical shapes of gLoG kernels (see Fig.6(b)), the summed gLoG filter $\nabla^2 G_s (x, y; \theta)$ is given by:

$$\nabla^2 G_s (x, y; \theta) = \frac{1}{S_k} \sum_{\sigma_x=\sigma_{\min}}^{\sigma_{\max}} \sum_{\sigma_y=\sigma_{\min}}^{\sigma_x} \nabla^2 G_n (x, y; \sigma_x, \sigma_y, \theta)$$
$$(14)$$

where S_k is the number of summed elliptical gLoG kernels. Note that $\nabla^2 G_s (x, y; \theta)$ is the summation of gLoG kernels in the orientation θ. Figs. 6(c)(d) show the corresponding summed results of gLoG kernels. With k orientations, there are $k+1$ summed gLoG kernels in total. For brevity, let us denote the summed gLoG kernels as $\nabla^2 G_s^j (x, y)$, where $j = 0 \ldots k$. The scale-space response map $L^j (x, y)$ is then obtained as:

$$L^j (x, y) = \overline{I} (x, y) * \nabla^2 G_s^j (x, y) \qquad (15)$$

Note that the response map $L^j (x, y)$ corresponds to the pattern matching result between the image and the gLoG kernel $\nabla^2 G_s^j (x, y)$.

Using $k + 1$ normalized gLoG kernels, there are $k + 1$ response images obtained by Eq. (15). Fig. 7(a) shows two touching nuclei with elliptical shapes and (major axis) directions about $45°$, while Figs. 7(b)-(f) show the response maps obtained by convolving Fig. 7(a) with gLoG kernels in Figs. 6(c)(d), respectively. In Figs. 7(b)-(f) the local maxima (usually round nuclei centers) are also searched and superimposed on the image with (red) plus symbols. As observed in Fig. 7, only the response map (d) provides two local maxima points, which correctly identifies the existence of two nuclei. By contrast, nuclei are not correctly detected from response maps (b)(c)(e)(f). Fig. 7(d) provides a correct detection, mainly because the gLoG kernel used in (d) has a similar direction with nuclei in (a). More details about searching nuclei seeds from multiple response maps will be presented in the next section.
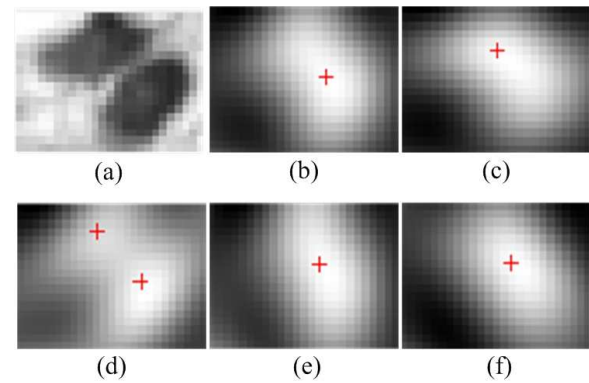

Fig. 7. Response maps with local maxima. (a) Two touching nuclei. (b)-(f) Response maps obtained by convolving (a) with gLoG kernels in Figs. 6(c)(d), respectively. Note that nuclei are correctly detected in image (d) which has two local maxima points indicating the existence of nuclei.

C. Nuclei Seeds Detection

Using the above obtained response maps $L^j (x, y)$, nuclei seeds can be detected as the points of local maxima which are usually around nuclei centers. In this module, we present the process of determining nuclei seeds from multiple response maps, which consists of four main steps as follows.

1) Searching local maxima: We first search the points of local maxima from each response map $L^j (x, y)$. Let us denote them as $\{B_i\}_{i=1 \ldots M}$, where M is the number of local maxima in $k + 1$ response maps. Fig. 8(a) shows the image $I (x, y)$ overlapped with local maxima (red + symbols).
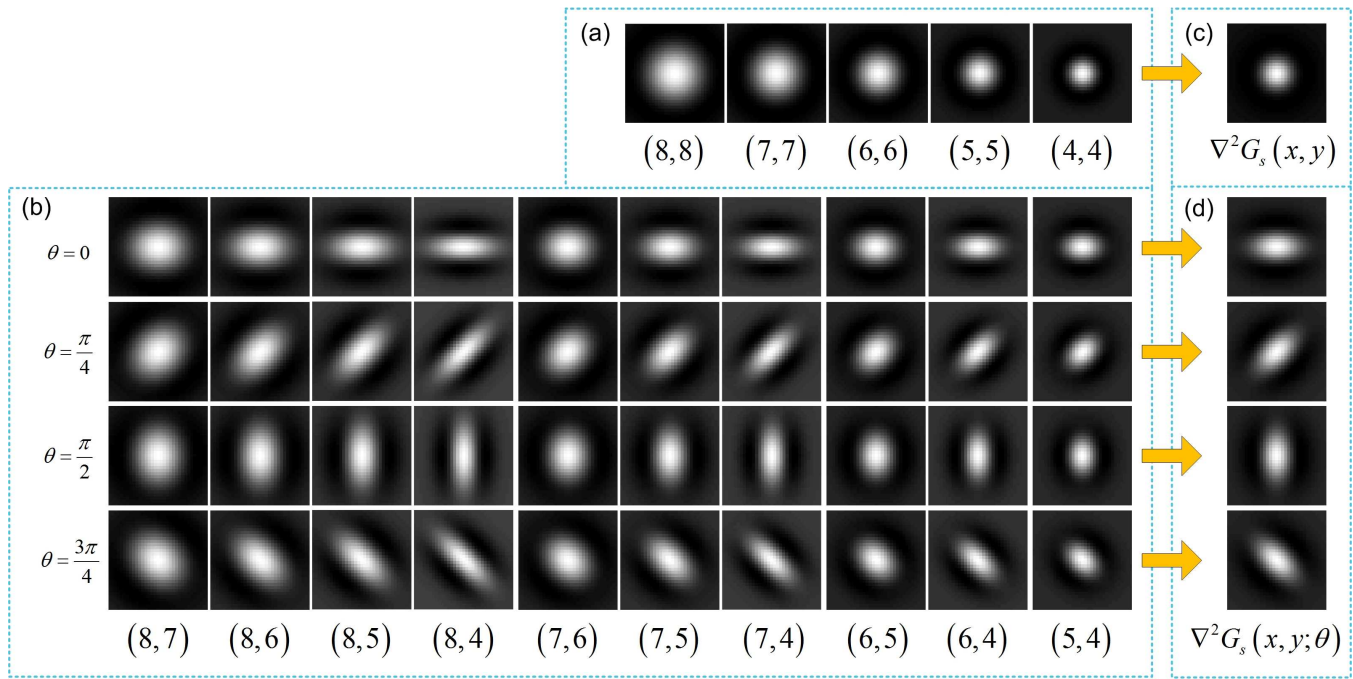
Fig. 6. Example of normalized gLoG kernels (with $k = 4$). (a) Rotational symmetric LoG kernels with $\sigma_x = \sigma_y \in \{8, 7, 6, 5, 4\}$. (b) gLoG kernels with $\theta \in \{0°, 45°, 90°, 135°\}$, $\sigma_x \in \{8, 7, 6, 5\}$, $\sigma_y \in \{7, 6, 5, 4\}$ and $\sigma_x > \sigma_y$. (c) $\nabla^2 G_s(x, y)$ (see Eq. (13)). (d) $\nabla^2 G_s(x, y; \theta)$ (see Eq. (14)). Note that in (a) and (b) $(\cdot, \cdot)$ corresponds to (σ_x, σ_y).

2) Filtering false local maxima: To filter out false local maxima in image background, we first apply the adaptive thresholding based technique [28] to perform image binarization. The adaptive thresholding based technique has two passes of Otsu's thresholding. In the first pass, Otus's thresholding is applied on the whole image $I(x, y)$, which segments nuclei regions into foreground. In the second pass, the bounding box (i.e., the smallest rectangle containing the region) for each foreground region is computed, and the pixels (retrieved from the image $I(x, y)$) within the bounding box are adaptively classified by Otsu's method. Note that two passes of Otsu's thresholding are sequentially applied which can reduce the impact of image variations on image binarization. After adaptive thresholding, a binary mask b_1 is generated with nuclei pixels as foreground. The local maxima $\{B_i\}_{i=1...M}$, which are in the background of mask b_1 are then eliminated, as they are generated due to the local noise in the image background. Let us denote the local maxima after this step as $\{B_i\}_{i=1...N}$, where N is the number of local maxima. In Fig. 8(a), the local maxima generated due to the local noise are highlighted by the (blue) circles. Fig. 8(b) shows the image $I(x, y)$ with local maxima $\{B_i\}_{i=1...N}$. Note that in Fig. 8(b) the (green) contours of nuclei regions are obtained after image binarization by adaptive thresholding.

3) Clustering local maxima: As observed in 8(b), there are usually more then one point of local maxima for each nuclei region. In other words, it exists redundant detections of cell nuclei by searching local maxima from multiple response maps. But it is also noted that the local maxima corresponding to each nucleus usually cluster together with a closely geometrical distance. This is because the locations of detected nuclei seeds are mainly determined by the scales of gLoG kernels.

In section B, we generate the aggregated gLoG filters based on the same set of σ_x and σ_y for any specific orientation θ, and hence different orientation of responses can generate closely located local maxima. Fig. 9 illustrates an example of seeds detection by different gLoG filters. In Fig. 9(a), the gLoG filters $\sigma_x = 8$, $\sigma_y = 7$, $\theta = \{45°, 90°\}$ are used, while in Fig. 9(b) the gLoG filters $\sigma_x = 8$, $\sigma_y = 7$, $\theta = 45°$ and $\sigma_x = 5$, $\sigma_y = 4$, $\theta = 45°$ are used. As observed in Fig. 9(a), the generated nuclei seeds are close with each other mainly due to the same scales of gLoG filters used. By contrast, the nuclei seeds in Fig. 9(b) are far away from each other as the scales of gLoG filters differ greatly.
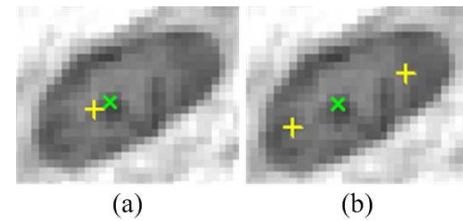

Fig. 9. Nuclei seeds detected by (a) gLoG filters $\sigma_x = 8$, $\sigma_y = 7$, $\theta = 45°$ (shown as ×) and $\sigma_x = 8$, $\sigma_y = 7$, $\theta = 90°$ (shown as +), (b) gLoG filters $\sigma_x = 8$, $\sigma_y = 7$, $\theta = 45°$ and $\sigma_x = 5$, $\sigma_y = 4$, $\theta = 45°$ (shown as +). Note that nuclei seeds detected by gLoG filters with the same scales are close with each other in (a).

To cluster the local maxima, we apply the mean-shift algorithm [29] on N local maxima points $\{B_i\}_{i=1...N}$ and group them based on their geometric closeness such that each nucleus corresponds to one cluster of local maxima. The bandwidth w of mean-shift algorithm is determined based on estimated radius of nuclei (e.g., 6 pixels in Fig. 8). Let the number of clusters be denoted by p after this step, and the p
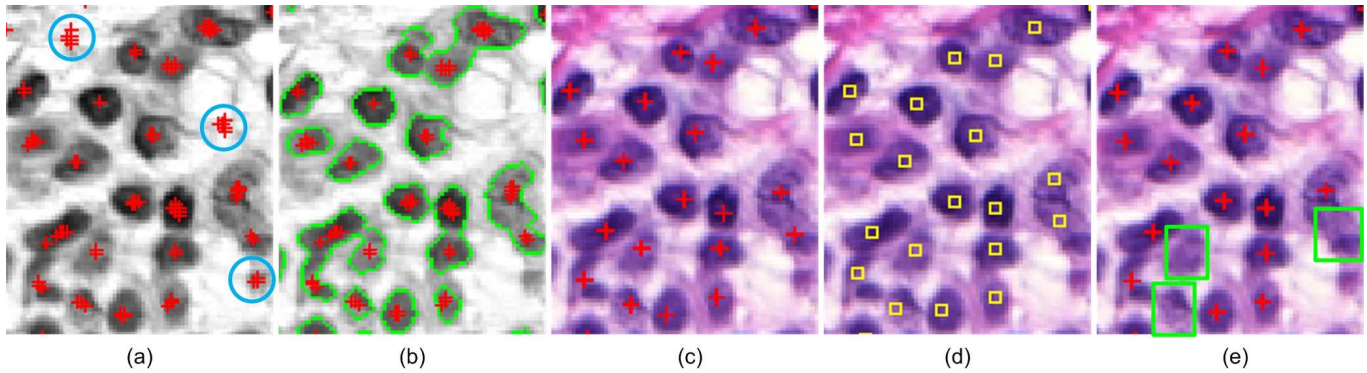
Fig. 8. Illustration of nuclei detection. (a) $I(x,y)$ with all local maxima (shown as +). (b) $I(x,y)$ with filtered local maxima (shown as +). (c) Original image with detected nuclei seeds by the proposed technique. (d) Original image with ground truths (shown as □). (e) Original image with detected seeds by the technique in [21]. Note that in (a) the circles indicate the local maxima generated by noise in the image background. In (b) nuclei contours are obtained by image binarization by adaptive thresholding. In (e) the rectangles highlight the missed nuclei (without seeds).

clusters be denoted by $\mathcal{T}_l, 1 \leq l \leq p$.

4) Identifying nuclei seeds: Since each nucleus corresponds to one cluster of local maxima, it is necessary to determine one point as nucleus seed. In this work, the point which has the maximum response value (retrieved from the corresponding response image $L^j(x,y)$ obtained in Eq. (15)) is selected as the nucleus seed from each cluster $\mathcal{T}_l, 1 \leq l \leq p$. Fig. 8(c) shows the original RGB image with the detected nuclei seeds (+ symbols) by the proposed technique, and Fig. 8(d) shows the manually labeled ground truths. Fig. 8(e) shows the original image with nuclei seeds detected by the blob location algorithm in [21], where the missed nuclei are highlighted by rectangles. As observed in Figs. 8(c)(d)(e), the proposed technique provides a more accurate nuclei detection, even for nuclei with light stains. In comparison, the technique in [21] misses several nuclei (i.e., without seeds), which do not have peak responses in the aggregated response map.

Once nuclei seeds are detected, we can easily estimate the orientation and scales of cell nuclei. Let us denote the detected nuclei seeds as $C_l, 1 \leq l \leq p$. Assume that the nucleus seed C_l corresponds to a peak response searched in the response map $L^j(x,y)$ (see Eq. 15), and the orientation of the aggregated gLoG kernel ($\nabla^2 G_s^j(x,y)$) is considered as the orientation of the nucleus. The aggregated gLoG kernel $\nabla^2 G_s^j(x,y)$ is summed from the same directional gLoG filters. Let us assume that the $\nabla^2 G_s^j(x,y)$ is obtained by summing S normalized gLoG kernels $\nabla^2 G_n(x,y)$ (see Eqs (13), (14)). To estimate the scales of nuclei, we can separately convolve the nuclei with each gLoG kernel $\nabla^2 G_n(x,y)$ to obtain S response maps. The response map that has the highest response value at the nucleus seed point C_l is selected, and the corresponding scales of the gLoG kernel $\nabla^2 G_n(x,y)$ are estimated as the nucleus scales. Fig 10(a) illustrates an example of nuclei scales estimation. The overlapped ellipses have a semi-major axis of $\sqrt{2}\widehat{\sigma_x}$, a semi-minor axis of $\sqrt{2}\widehat{\sigma_y}$ and an orientation of $\widehat{\theta}$, where $\widehat{\sigma_x}$, $\widehat{\sigma_y}$ and $\widehat{\theta}$ are the estimated scales and orientations of nuclei. Using the detected seeds as markers, nuclei boundaries can also be efficiently obtained by marked watershed algorithm [5] or level set algorithm [4]. Fig. 10(b) shows the nuclei segmentation by the marked watershed algorithm. Note that the nuclei boundary detection is beyond the main scope of this work, and for more

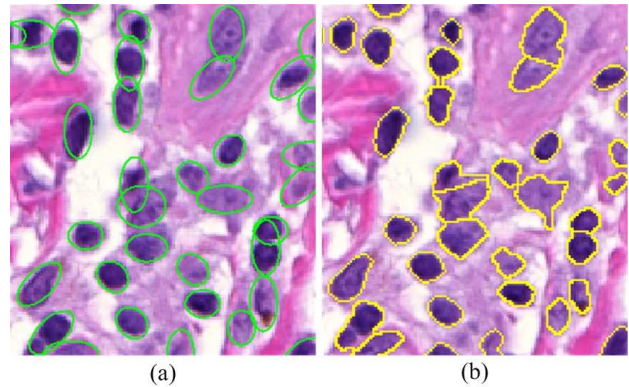details please refer to the corresponding references [4], [5].

Fig. 10. Nuclei scales estimation and segmentation. (a) Nuclei ellipses generated based scales and orientation estimation. (b) Marked watershed segmentation.

IV. EXPERIMENTAL RESULTS

To evaluate the performance of the proposed technique, we carried out a series of experiments using datasets I and II. The main objective of evaluation is to determine if the automatically detected nuclei seeds are consistent with the manually labeled ground truths. In this section, we present the nuclei detection performance of the proposed technique and compare it with several existing techniques.

A. Parameters Configuration and Comparisons

There are four parameters that should be determined appropriately in the proposed technique. Since cell nuclei in datasets I and II have similar size variations, we have used the same set of parameter values for two datasets. Table III lists the parameters and corresponding values for our technique. The parameter k determines the orientations of gLoG kernels, which is set as 9 (i.e., nine orientations: $\theta = m\pi/9, \ m = 0, \ldots, 8$) with an angular resolution of $20°$. The parameters $\sigma_{\min}$ and $\sigma_{\max}$ are determined based on the relationship between the radius r of detected objects and scales of gLoG kernels $\sqrt{2}\sigma_{\min} \leq r \leq \sqrt{2}\sigma_{\max}$ [26]. Here we measure the minimal

TABLE III
PARAMETERS CONFIGURATION IN THE PROPOSED TECHNIQUE.

Parameters	k	$\sigma_{\min}$	$\sigma_{\max}$	w
Values	9	4	8	6

and maximal radii $(r_{\min}, r_{\max})$ of nuclei (in pixels) in several manually labeled nuclei regions, and set $\sigma_{\min}$ and $\sigma_{\max}$ as $r_{\min}/\sqrt{2}$ and $r_{\max}/\sqrt{2}$, respectively. The bandwidth w of the mean-shift algorithm is empirically set as the minimal radius $r_{\min}$ of detected objects.

We compare the proposed technique with several existing techniques for blob (e.g., cell nuclei) detection. These techniques include the restricted randomized hough transform (RRHT) [30], DoG filters with blobness measure [16], mLoG based method [18], gLoG based method [21], and voting based method [5]. The parameters of these methods are mainly determined by the estimated nuclei size (i.e., nuclei radii range). In our comparisons, we have experimentally set the optimal parameter values for these techniques such that the best performance is achieved with our testing images. It should be mentioned that the original gLoG based method [21] is highly sensitive to the image noise which cannot be directly applied on our testing datasets. We have determined a threshold τ based on trial and error tests to filter out false seeds in the image background. In particular, if the points of local maxima searched from the aggregated response map have a response value above τ, they are considered as nuclei seeds. In this work, τ is set as 45. Figs. 11(a)(b) show the nuclei detection results by the technique in [21] before and after filtering false seeds by the threshold τ. As observed in Fig. 11, the threshold τ can effectively remove false seeds in the image background. To further verify the capabilities of identifying elliptical blobs by gLoG kernels, we also combined the traditional circular LoG kernels [14] with our post-pruning methods (based on adaptive thresholding and mean-shift clustering) to conduct nuclei seeds detections (henceforth refereed to as the LoG+PP technique). All experimental results of these methods are to be provided in following subsections.
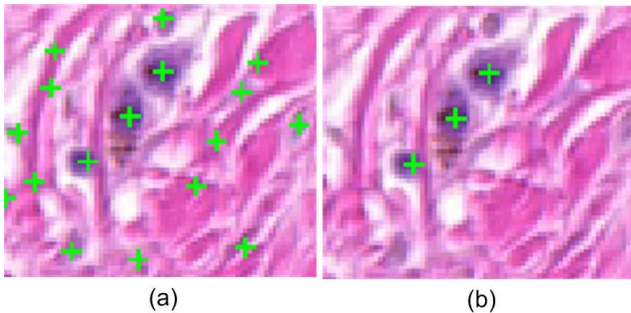

Fig. 11. Nuclei detection results by the technique in [21]. (a) Results before filtering false seeds. (b) Results after filtering false seeds.

B. Performance Evaluation

To evaluate the nuclei detection performance, the automatically detected nuclei seeds are compared with the manually labeled ground truths (provided by pathologists). An automatically detected seed s_i is counted as a true positive (TP) if and only if its location is in a detection pair (s_i, g_j) for which the corresponding (nearest) ground truth seed g_j has not been paired [31], and also their Euclidean distance is within a certain range of d (number of pixels). Fig. 12 illustrates examples of TPs and false positives (FPs). Figs. 12(a)(b) show two simple examples of TP and FP, respectively. In Fig. 12(c), s_1 is counted as a TP because it has the closest distance (smaller than d) with g_1, whereas s_2 is counted as a FP because g_1 has been used and paired with s_1. In Fig. 12(d), if $d_1 < d_2 < d_3$, s_1 is paired with g_1 and counted as a TP. Meanwhile s_2 is paired with g_2 and counted as a TP. However, if $d_2 < d_1 < d_3$, s_1 is paired with g_2 and counted as a TP, but s_2 is now counted as a FP.
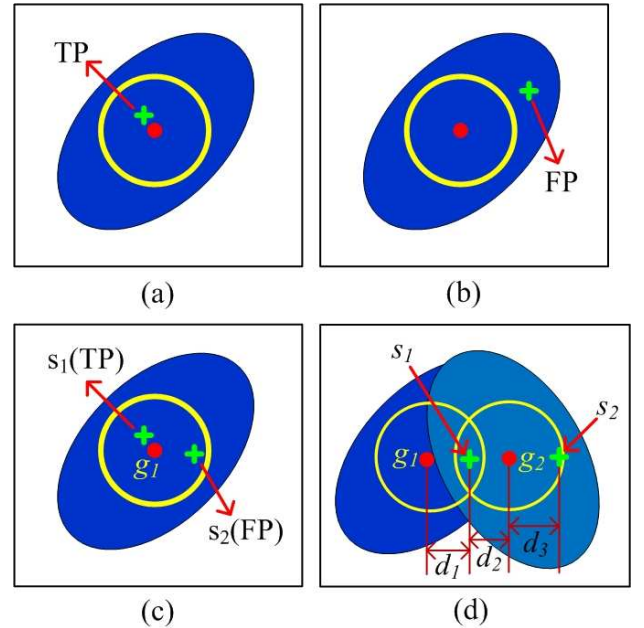

Fig. 12. Definition of true positives and false positives. Note that in (d) d_1, d_2 and d_3 are the Euclidean distances corresponding to different pairs of points.

Let N_{GT}, N_{DS} and N_{TP} denote the numbers of ground truth seeds, detected seeds and true positives seeds, respectively. The performance is evaluated with respect to the recall ($\mathcal{D}_{REC}$), precision ($\mathcal{D}_{FRE}$) and F-measure ($\mathcal{D}_F$) which are defined as follows:

$$\mathcal{D}_{REC} = \frac{N_{TP}}{N_{GT}} \times 100\% \tag{16}$$

$$\mathcal{D}_{FRE} = \frac{N_{TP}}{N_{DS}} \times 100\% \tag{17}$$

$$\mathcal{D}_F = \frac{2 \times (\mathcal{D}_{REC} \times \mathcal{D}_{PRE})}{(\mathcal{D}_{REC} + \mathcal{D}_{PRE})} \tag{18}$$

Table IV shows the quantitative evaluations of nuclei detection performance for the proposed technique and existing techniques, where the distance d is set as 6 pixels. Note that F-measure $\mathcal{D}_F$ is the harmonic mean of precision and recall, which provides a comprehensive measurement of the performance. It is observed in Table IV that the proposed technique

TABLE IV
COMPARISON OF NUCLEI DETECTION PERFORMANCE ($d = 6$).

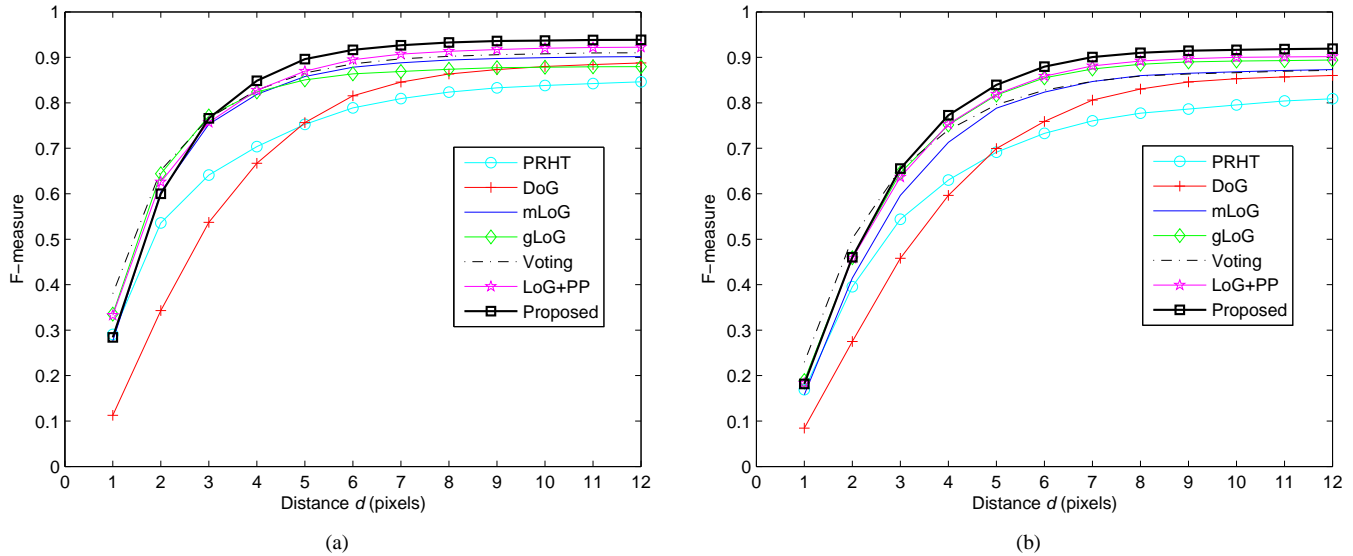| Techniques	Dataset-I						Dataset-II					
	N_{GT}	N_{DS}	$\mathcal{D}_{REC}(\%)$	$\mathcal{D}_{FRE}(\%)$	$\mathcal{D}_{F}(\%)$	t	N_{GT}	N_{DS}	$\mathcal{D}_{REC}(\%)$	$\mathcal{D}_{FRE}(\%)$	$\mathcal{D}_{F}(\%)$	t
RRHT [30]	7701	6613	72.97	85.94	78.89	13.0	6048	6553	76.42	70.74	73.27	7.3
DoG [16]	7701	8193	83.05	80.20	81.53	32.5	6048	6430	78.39	73.88	75.92	9.0
mLoG [18]	7701	7991	88.67	87.08	87.83	7.4	6048	6429	85.07	79.96	82.35	3.0
gLoG [21]	7701	7052	83.63	89.55	86.39	36.3	6048	5795	83.94	87.28	85.50	27.5
Voting [5]	7701	7400	86.17	91.21	88.58	606.4	6048	5893	81.81	83.91	82.76	306.8
LoG+PP	7701	7841	89.42	89.63	89.48	7.0	6048	6191	87.10	84.79	85.84	3.1
Proposed	7701	7424	89.45	94.20	91.72	11.3	6048	5963	87.44	88.42	87.87	6.7

Fig. 13.   F-measures with different distance d values. (a) Performances on dataset-I. (b) Performances on dataset-II.

achieves the highest F-measure for two testing datasets (on average 91.72% and 87.87%, respectively) among all techniques. The LoG+PP technique achieves a relatively poor performance compared to the proposed technique, but marginally better performance than other existing techniques. This indicates that the gLoG kernels are superior to traditional LoG kernels in detecting elliptical blobs, and our post-pruning algorithms based on mean-shift clustering and adaptive thresholding can efficiently remove false seeds. The RRHT technique [30] provides the poorest performance among all techniques for two datasets. This is mainly because Hough transform is performed on the edge detected image, and inaccurate edge detection has significantly negative influence on nuclei seeds detection. The other existing techniques have the intermediate F-measure values. Their performance are mainly limited by either consideration of nuclei as circular blobs or filtering of false seeds using unstable post-pruning approaches. Fig. 13 compares nuclei seeds detection performance with respect to F-measures of different techniques, where the distance d is ranged from 1 to 12 pixels. As observed in Fig. 13, the performance of different techniques except the DoG technique [16] is similar when $d < 3$. Since the DoG filters are the approximation of LoG operators, they are not accurate in locating nuclei centers and have a poorer performance when d has small values.

Comparatively, the proposed technique provides a markedly superior performance when $d \geq 3$. The proposed technique makes use of directional information of gLoG kernels and searches potential nuclei seeds from multiple response maps, which provides a more accurate nuclei detection.

For visual comparison, Fig. 14 shows two randomly cropped image patches with nuclei seeds detected by different techniques. In Fig. 14, the first row shows a skin image and the second row shows a breast image. The automatically detected nuclei seeds are indicated by + symbols, while the ground truths (in the last column) are indicated by □ symbols. The rectangles in the images highlight the missed or false seeds generated by computerized methods. As observed in Fig. 14, the proposed technique provides a superior performance in nuclei detections, which has lower false and missed detections than existing techniques. Although a good performance is achieved by the proposed technique, it still has failure cases when nuclei are closely clustered together (see highlighted regions in Fig. 14(g)). If the nuclei are severely clustered together, it is actually very difficult to be identified even by the experienced pathologists. Fig. 15(a) shows nuclei detection results in a skin image, and Fig. 15(b) shows two zoomed in image patches for better illustration. As seen in Fig. 15, the proposed technique can detect most nuclei correctly.
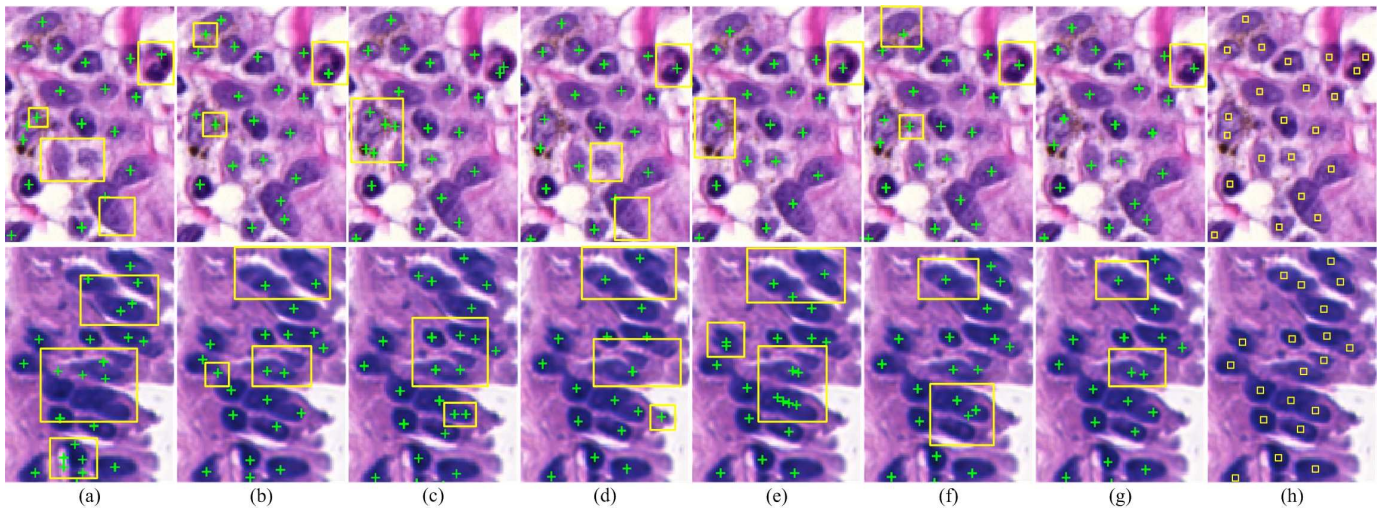
Fig. 14. Nuclei detection in skin (first row) and breast (second row) images. (a) RRHT[30], (b) DoG[16], (c) mLoG[18], (d) gLoG[21], (e) Voting[5], (f) LoG+PP, (g) Proposed technique, and (h) Ground truths. Note that automatically detected nuclei seeds are indicated by plus symbols, while ground truths in the last column are indicated by squares. The missing or false seeds are highlighted with rectangles.
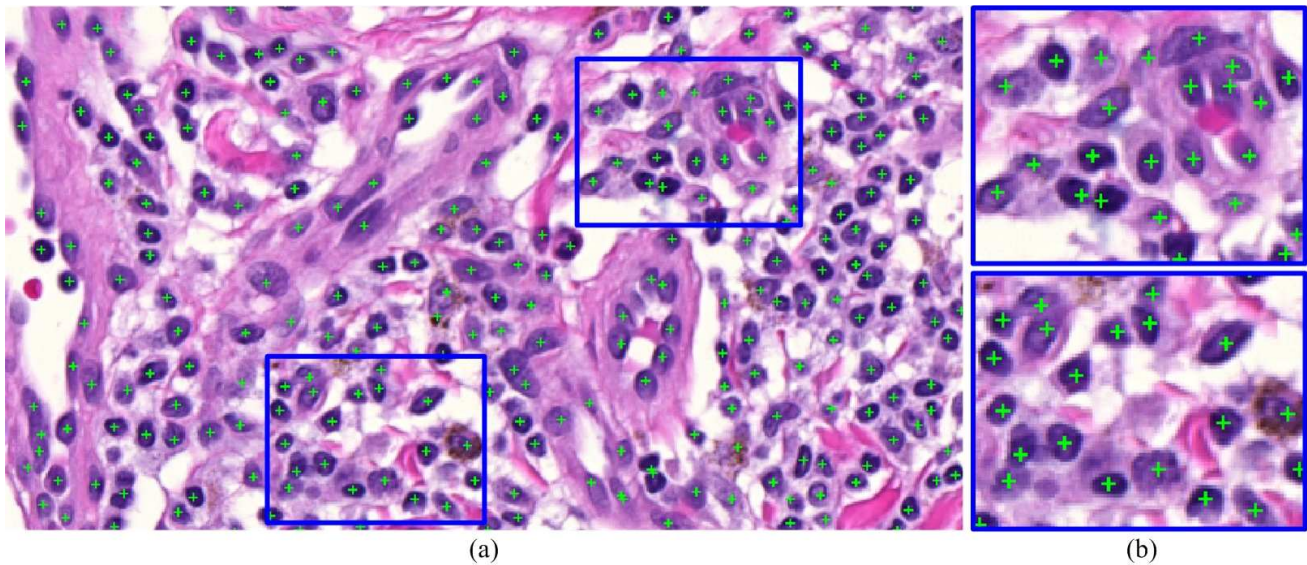

Fig. 15. Nuclei detection by the proposed technique. (a) A skin image with detected seeds. (b) Zoomed in image patches.

C. Parameter Sensitivities Evaluation

As listed in Table III, there are four key parameters that should be pre-defined. Parameters $\sigma_{\min}$ and $\sigma_{\max}$ can be optimally determined based on the average radius of detected nuclei. Parameter k determines the angular resolution of gLoG kernels, which is empirically set as 9 (corresponds to $20°$ angular resolution). To evaluate the sensitivity of this parameter, we further test k with values $\{7, 8, 10, 11\}$ on two datasets. Fig. 16(a) shows the F-measures with different k values on two datasets. As seen in Fig. 16(a), the F-measures for the same dataset are similar with different k values. This indicates that the proposed technique is generally robust to choice of parameter k. However, note that since k determines the angular resolution of gLoG kernels, with a larger k value, more accurate estimation of nucleus' orientation will be obtained. Another parameter in our technique is the bandwidth w of

mean-shift algorithm which is used for post-pruning to merge redundant seeds. The parameter w is empirically set as the minimal nuclei radius (i.e., $w = 6$ pixels in this work). To evaluate the sensitivity of this parameter, we varied w by 10% and 20% around 6 (or tuned it from 4.8 to 7.2 with a step of 0.6). Fig. 16(b) shows the F-measures with respect to different w values on two datasets. As observed in Fig 16(b), the F-measures only have marginal fluctuations, and hence it can be concluded that the proposed technique is not sensitive to the parameter w when a reasonable value is selected.

D. Computational Complexity and Limitations

To evaluate the computational complexity, the average run time t on two datasets is separately calculated. All our experiments were carried out on a 2.9-GHz CPU with 4 GB RAM using MATLAB R2013a. In Table IV, the 7th and 13th columns show the values of t for different techniques
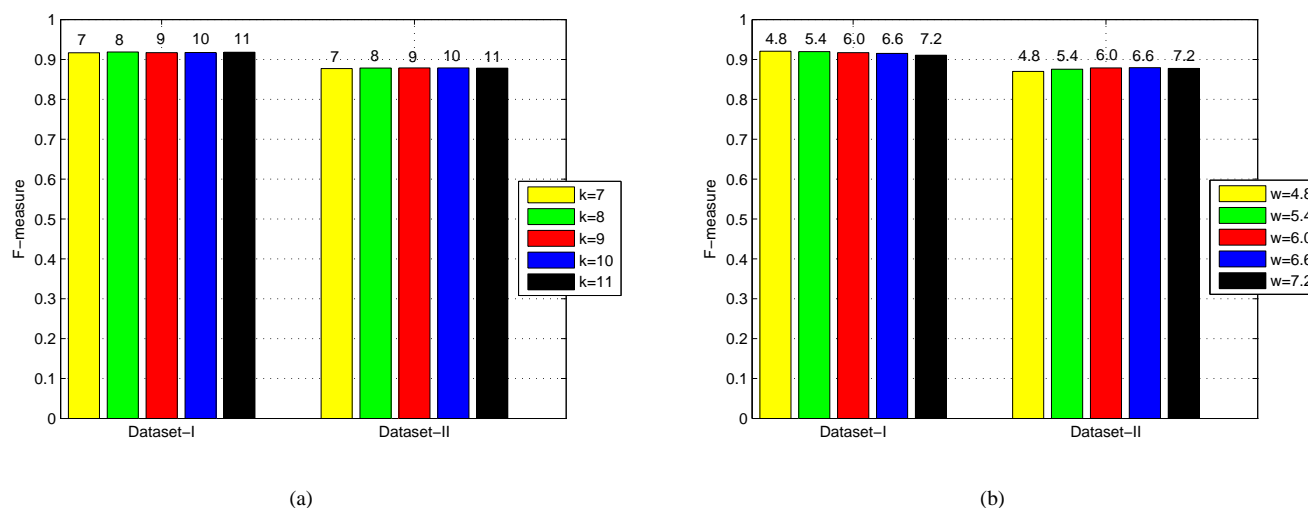
Fig. 16. F-measures with different parameter settings. (a) $k = \{7, 8, 9, 10, 11\}$. (b) $w = \{4.8, 5.4, 6.0, 6.6, 7.2\}$.

on dataset-I and II, respectively. It is observed in Table IV that the voting technique [5] has the highest computational complexity (606.4s and 306.8s), which is significantly low-efficient compared to other techniques. The next is the gLoG technique [21] which is roughly a few times compute-intensive than other techniques. The proposed technique is motivated by the gLoG technique in [21], but it is about three times faster than that in [21]. This is due to the accumulations of gLoG kernels with the same orientations before performing convolution operation, which reduces the number of convolutions (convolution takes a relatively long time for a large image).

It should also be mentioned that like every computerized method, the proposed technique also has limitations, which is generated during the accumulation of the same directional gLoG kernels. There may exist a peak response at a single s-cale, but no peak response may be detected when accumulating gLoG kernels together. This is because the total response might be pulled downed by a negative response at a single scale, even though the individual scales get a high value. However, based on our experience, this is unlikely to happen if we select the appropriate scales for gLoG filters.

V. CONCLUSION

This paper presents a robust nuclei detection technique based on directional gLoG kernels and mean-shift clustering for microscopic images. The proposed technique first construct a bank of different direction-and-scale gLoG kernels. These gLoG kernels are then summed together according to their orientations and convolved with the image to generate a set of response maps. The nuclei seeds are finally searched from the generated response maps with false seeds removed based on adaptive thresholding and redundant seeds merged based on mean-shift clustering. Experimental results on two datasets show that the proposed technique provides a superior performance in nuclei detection compared to existing techniques.

REFERENCES

[1] J. Byun, M. R. Verardo, B. Sumengen, G. P. Lewis, B. Manjunath, and S. K. Fisher, "Automated tool for the detection of cell nuclei in digital microscopic images: application to retinal images," *Molecular Vision*, vol. 12, pp. 949–960, 2006.

[2] C. Lu and M. Mandal, "Automated analysis and diagnosis of skin melanoma on whole slide histopathological images," *Pattern Recognition*, vol. 48, no. 8, pp. 2738–2750, 2015.

[3] S. Petushi, F. U. Garcia, M. M. Haber, C. Katsinis, and A. Tozeren, "Large-scale computations on histology images reveal grade-differentiating parameters for breast cancer," *BMC Medical Imaging*, vol. 6, no. 1, p. 14, 2006.

[4] X. Qi, F. Xing, D. J. Foran, and L. Yang, "Robust segmentation of overlapping cells in histopathology specimens using parallel seed detection and repulsive level set," *IEEE Transactions on Biomedical Engineering*, vol. 59, no. 3, pp. 754–765, 2012.

[5] H. Xu, C. Lu, and M. Mandal, "An efficient technique for nuclei segmentation based on ellipse descriptor analysis and improved seed detection algorithm," *IEEE Journal of Biomedical and Health Informatics*, vol. 18, no. 5, pp. 1729–1741, 2014.

[6] P. Yan, X. Zhou, M. Shah, and S. T. Wong, "Automatic segmentation of high-throughput rnai fluorescent cellular images," *IEEE Transactions on Information Technology in Biomedicine*, vol. 12, no. 1, pp. 109–117, 2008.

[7] H. Fatakdawala, J. Xu, A. Basavanhally, G. Bhanot, S. Ganesan, M. Feldman, J. E. Tomaszewski, and A. Madabhushi, "Expectation–maximization-driven geodesic active contour with overlap resolution (emagacor): Application to lymphocyte segmentation on breast cancer histopathology," *IEEE Transactions on Biomedical Engineering*, vol. 57, no. 7, pp. 1676–1689, 2010.

[8] O. Schmitt and S. Reetz, "On the decomposition of cell clusters," *Journal of Mathematical Imaging and Vision*, vol. 33, no. 1, pp. 85–103, 2009.

[9] B. Ehteshami Bejnordi, G. Litjens, N. Timofeeva, I. Otte-Holler, A. Homeyer, N. Karssemeijer, and J. van der Laak, "Stain specific standardization of whole-slide histopathological images," *IEEE Transactions on Biomedical Engineering*, 2015.

[10] M. N. Gurcan, T. Pan, H. Shimada, and J. Saltz, "Image analysis for neuroblastoma classification: Segmentation of cell nuclei," in *Proceeding of 28th Annual International Conference on Engineering in Medicine and Biology Society*. IEEE, 2006, pp. 4844–4847.

[11] J. Cheng and J. C. Rajapakse, "Segmentation of clustered nuclei with shape markers and marking function," *IEEE Transactions on Biomedical Engineering*, vol. 56, no. 3, pp. 741–748, 2009.

[12] C. Jung and C. Kim, "Segmenting clustered nuclei using h-minima transform-based marker extraction and contour parameterization," *IEEE Transactions on Biomedical Engineering*, vol. 57, no. 10, pp. 2600–2604, 2010.

[13] B. Parvin, Q. Yang, J. Han, H. Chang, B. Rydberg, and M. H. Barcellos-Hoff, "Iterative voting for inference of structural saliency and characterization of subcellular events," *IEEE Transactions on Image Processing*, vol. 16, no. 3, pp. 615–623, 2007.

[14] T. Lindeberg, "Feature detection with automatic scale selection," *International journal of computer vision*, vol. 30, no. 2, pp. 79–116, 1998.

[15] D. G. Lowe, "Object recognition from local scale-invariant features," in *Proceedings of the seventh IEEE international conference on computer vision*, vol. 2. IEEE, 1999, pp. 1150–1157.

[16] M. K. K. Niazi, A. A. Satoskar, and M. N. Gurcan, "An automated method for counting cytotoxic t-cells from cd8 stained images of renal biopsies," in *SPIE Medical Imaging*. International Society for Optics and Photonics, 2013, pp. 867 606–867 606.

[17] O. Sertel, B. Dogdas, C. S. Chiu, and M. N. Gurcan, "Microscopic image analysis for quantitative characterization of muscle fiber type composition," *Computerized Medical Imaging and Graphics*, vol. 35, no. 7, pp. 616–628, 2011.

[18] Y. Al-Kofahi, W. Lassoued, W. Lee, and B. Roysam, "Improved automatic detection and segmentation of cell nuclei in histopathology images," *IEEE Transactions on Biomedical Engineering*, vol. 57, no. 4, pp. 841–852, 2010.

[19] K. Okada, D. Comaniciu, and A. Krishnan, "Scale selection for anisotropic scale-space: application to volumetric tumor characterization," in *Proceedings of the IEEE Computer Society Conference on Computer Vision and Pattern Recognition*, vol. 1. IEEE, 2004, pp. I–594.

[20] K. Mikolajczyk and C. Schmid, "An affine invariant interest point detector," in *Computer VisionECCV 2002*. Springer, 2002, pp. 128–142.

[21] H. Kong, H. C. Akakin, and S. E. Sarma, "A generalized laplacian of gaussian filter for blob detection and its applications," *IEEE Transactions on Cybernetics*, vol. 43, no. 6, pp. 1719–1733, 2013.

[22] R. Gonzalez and R. Woods, *Digital image processing*, 3rd, Ed. USA: Prentice Hall, 2008.

[23] M. Zhang, T. Wu, and K. M. Bennett, "Small blob identification in medical images using regional features from optimum scale," *IEEE Transactions on Biomedical Engineering*, vol. 62, no. 4, pp. 1051–1062, 2015.

[24] C. for Bio-Image Informatics, "Bio-segmetnation," website, November 2015. [Online]. Available: http://bioimage.ucsb.edu/

[25] H. Xu and M. Mandal, "Epidermis segmentation in skin histopathological images based on thickness measurement and k-means algorithm," *EURASIP Journal of Image and Video Processing*, vol. 2015, no. 1, pp. 1–14, 2015.

[26] J. Stegmaier, J. C. Otte, A. Kobitski, A. Bartschat, A. Garcia, G. U. Nienhaus, U. Strähle, and R. Mikut, "Fast segmentation of stained nuclei in terabyte-scale, time resolved 3d microscopy image stacks," *PloS one*, vol. 9, no. 2, p. e90036, 2014.

[27] C. Xiao, M. Staring, Y. Wang, D. P. Shamonin, and B. C. Stoel, "Multiscale bi-gaussian filter for adjacent curvilinear structures detection with application to vasculature images," *IEEE Transactions on Image Processing*, vol. 22, no. 1, pp. 174–188, 2013.

[28] C. Lu and M. Mandal, "Toward automatic mitotic cell detection and segmentation in multispectral histopathological images," *IEEE Journal of Biomedical and Health Informatics*, vol. 18, no. 2, pp. 594–605, 2014.

[29] D. Comaniciu and P. Meer, "Mean shift: A robust approach toward feature space analysis," *IEEE Transactions on Pattern Analysis and Machine Intelligence*, vol. 24, no. 5, pp. 603–619, 2002.

[30] Z. Cheng and Y. Liu, "Efficient technique for ellipse detection using restricted randomized hough transform," in *Proceedings of International Conference on Information Technology: Coding and Computing*, vol. 2. IEEE, 2004, pp. 714–718.

[31] M. Zhang, T. Wu, S. Beeman, L. Cullen-McEwen, J. Bertram, J. Charlton, E. Baldelomar, and K. Bennett, "Efficient small blob detection based on local convexity, intensity and shape information," *IEEE Transactions on Medical Imaging*, 2015.

Hongming Xu received his B.Sc. and M.Sc. degree in Computer Engineering from Information Engineering College, Northwest A&F University, Shaanxi, China, in 2009 and 2012. He is currently working toward his PhD degree in electrical engineering in the Multimedia Computing and Communication Lab, Department of Electrical Engineering, University of Alberta, Edmonton, AB, Canada, from 2012 till now. Mr. Xu is the recipient of the Chinese Scholarship Council and AITF award in Alberta for his PhD studies. His research interest includes medical image analysis, pattern recognition and computer vision.

Cheng Lu received his B.Sc. and M.Sc. degree in Computer Engineering from Information Engineering College, Northwest A&F University, Shaanxi, China, in 2006 and 2008. He received his Ph.D. degree in Electrical and Computer Engineering in University of Alberta, Edmonton, AB, Canada in 2013. He is now working as a research associate in Center for Computational Imaging & Personalized Diagnostics, Case Western Reserve University, US. His research interest includes computer vision, medical image analysis, pattern recognition and super resolution imaging.

Richard Berendt attended medical school at the University of Alberta in Edmonton, Alberta, Canada. He was then accepted into the Laboratory Medicine and Pathology residency program at the University of Alberta. Dr. Berendt is certified in both Clinical Pathology and Anatomic Pathology and General Pathology and Anatomical Pathology in Canada.

Naresh Jha received the Bachelor of Medicine and Bachelor of Surgery degrees from Delhi University, India, in 1979. He became a Fellow of the Royal College of Physicians of Canada in Radiation Oncology in 1987. Since 1988 he has been a Senior Radiation Oncologist at the Cross Cancer Institute, University of Alberta, Edmonton, AB, Canada. He specializes in head and neck, thyroid, and skin cancers. He is also a pioneer of the submandibular salivary gland transfer which is a ground breaking technique to prevent radiation-induced xerostomia.

Mrinal Mandal is a Full Professor and Associate Chair in the Department of Electrical and Computer Engineering and is the Director of the Multimedia Computing and Communications Laboratory at the University of Alberta, Edmonton, Canada. He has authored the book Multimedia Signals and Systems (Kluwer Academic), and coauthored the book Continuous and Discrete Time Signals and Systems (Cambridge University Press). His current research interests include Multimedia, Image and Video Processing, Multimedia Communications, Medical Image Analysis. He has published over 140 papers in refereed journals and conferences, and has a US patent on lifting wavelet transform architecture. He has been the Principal Investigator of projects funded by Canadian Networks of Centers of Excellence such as CITR and MICRONET, and is currently the Principal Investigator of a project funded by the NSERC. He was a recipient of Canadian Commonwealth Fellowship from 1993 to 1998, and Humboldt Research Fellowship from 2005-2006 at Technical University of Berlin.